Journal of Inorganic Biochemistry 191 (2019) 8–20

Contents lists available at ScienceDirect

Journal of Inorganic Biochemistry

journal homepage: www.elsevier.com/locate/jinorgbio

Synthesis and structural characterization of antimicrobial binuclear copper (II) coordination compounds bridged by hydroxy- and/or thiodipropionic acid

Hana Buchtelova[a], Zuzana Skubalova[a], Vladislav Strmiska[a], Petr Michalek[a,b], Silvia Kociova[a], Kristyna Smerkova[a,b], Rafal Kruszynski[c], Alina Bienko[d], Michalina Kaj[d], Agnieszka Lewinska[d], Dariusz Bienko[e], Magdalena Malik-Gajewska[e], Vedran Milosavljevic[a,b], Pavel Kopel[a,b], Zbynek Heger[a,b], Vojtech Adam[a,b,*]

[a] Department of Chemistry and Biochemistry, Mendel University in Brno, Zemedelska 1, CZ-613 00 Brno, Czech Republic
[b] Central European Institute of Technology, Brno University of Technology, Purkynova 656/123, CZ-612 00 Brno, Czech Republic
[c] Department of X-ray Crystallography and Crystal Chemistry, Institute of General and Ecological Chemistry, Lodz University of Technology, Zeromskiego 116, PL-90-924 Lodz, Poland
[d] Faculty of Chemistry, University of Wroclaw, 14 F. Joliot-Curie, PL-50-383 Wroclaw, Poland
[e] Faculty of Chemistry, Wroclaw University of Technology, Wybrzeze Wyspianskiego 27, PL-50-370 Wroclaw, Poland

ARTICLE INFO

Keywords:
Antimicrobial agents
Biocompatibility
Copper coordination compounds
Methicillin-resistant *Staphylococcus aureus*
Magnetic properties

ABSTRACT

In the present study, two binuclear copper(II) coordination compounds bridged by hydroxy- and thiodipropionic acid have been synthesized. The structure of compounds was determined by X-ray crystallography. The central copper atoms exist in square pyramidal surroundings. Basal plane is formed by nitrogen atoms of amines and oxygen atoms of bridges, whereas apical positions are occupied by oxygen atoms of coordinated water molecules. Temperature dependence study of magnetic susceptibility proved strong antiferromagnetic exchange between copper atoms in hydroxy-bridged complex. These coordination compounds were also tested for their biological activities *in vitro*. Both coordination compounds exhibit pronounced cytocompatibility in mammalian epithelial cells with no induction of oxidative stress and DNA fragmentation. Moreover, synthesized compounds are hemocompatible and do not alter expression of a marker of multiple cellular stress, p53. On the other hand, both compounds had stimulatory effect on expression of metallothioneins (MT-1/2 and MT-3). Antimicrobial testing on *Escherichia coli*, *Staphylococcus aureus* and methicillin-resistant *Staphylococcus aureus* revealed that both copper compounds exhibit antibacterial activity regardless the cell wall composition. Overall, current work presents a synthesis of Cu(II) coordination compounds with interesting biological behavior and with a promising potential to be further tested in pre-clinical models.

1. Introduction

Copper exhibits considerable biochemical activity either as an essential trace metal or as a constituent of various exogenously administered compounds. Any excess of Cu beyond physiological capacity may be misallocated to nonspecific and low-affinity metal ion binding sites that results in inactivation of crucial enzymes and interference with normal metabolism [1]. In the field of medicinal bioinorganic chemistry, Cu compounds have been the subject of numerous reports demonstrating activity of Cu against viruses, bacteria or fungi or as central atom in various anticancer drugs [2–4]. Due to its bacteriostatic activity, Cu is commonly present in touch surfaces used in hospitals and healthcare setting, disallowing the growth and transfer of bacteria [5,6]. In cancer therapy, copper coordination compounds are reported to have a broader spectrum of activities circumventing inherited and/or acquired resistance to platinum drugs [7–9]. From such compounds, structurally determined copper coordination compounds with bridging thiodiacetic acid (H_2tda) are known [10–12]. On the basis of these molecular structures it can be stated that thiodiacetate anion can coordinate Cu in different coordination modes and sulfur atom can be involved in coordination, too. It is interesting to compare these compounds with those possessing a longer carboxylate bridge chain, namely

* Corresponding author at: Department of Chemistry and Biochemistry, Mendel University in Brno, Zemedelska 1, CZ-613 00 Brno, Czech Republic.
E-mail address: vojtech.adam@mendelu.cz (V. Adam).

https://doi.org/10.1016/j.jinorgbio.2018.10.011
Received 23 August 2018; Received in revised form 19 October 2018; Accepted 23 October 2018
Available online 06 November 2018
0162-0134/

with thiodipropionic acid (H_2tdpa), which was studied by Arici et al. [13–15].

The current study focuses on a synthesis, characterization and biological testing of two binuclear Cu(II) coordination compounds with amines [*N*,*N*,*N′*,*N″*,*N″*-pentamethyldiethylenetriamine (pmdien) and *N*,*N*,*N′*,*N′*-tetramethylethane-1,2-diamine (tmen)] bridged by thiodipropionic acid or by hydroxo groups that are well known for their biocompatibility in mammalian cells [16,17]. The amines were chosen because of their steric hindrance caused by the presence of methyl groups. On the other side, hydrogens of methyl groups can be involved in hydrogen bonding with biomolecules. Using the synthesized and characterized coordination compounds, an array of biological tests was performed to reveal cytotoxicity in mammalian epithelial cells as well as antimicrobial activity especially for methicillin-resistant *Staphylococcus aureus* (MRSA).

2. Experimental

2.1. Chemicals and methods

Chemicals were purchased from Sigma-Aldrich (St. Louis, MO, USA) in ACS purity, unless noted otherwise. C, H, N, and S were determined on EA 1108 instrument (Fisons, Loughborough, UK).

2.2. Procedure for synthesis of **1** and **2**

$[Cu_2(pmdien)_2(H_2O)_2(\mu\text{-}tdpa)](ClO_4)_2{\cdot}H_2O$ (**1**)

The ligand pmdien (0.2 mL, 1 mmol) was added to a stirred solution of $Cu(ClO_4)_2{\cdot}6H_2O$ (0.36 g, 1 mmol) in methanol (40 mL). Solution of H_2tda (0.089 g, 0.5 mmol) neutralized with KOH (0.056 g, 1 mmol) in water (5 mL) was added. Blue color turned to violet and white precipitate formed was removed by filtration. The filtrate was left for crystallization. After a week blue crystals (suitable for X-ray analyses) were collected, washed with methanol and dried in air. Yield: 345 mg, 77%. Anal. calcd. ($C_{24}H_{60}N_6O_{15}SCl_2Cu_2$): C, 31.9; H, 6.7; N, 9.3; S, 3.5 Found: C, 31.7; H, 6.7; N, 9.2; S, 3.3%.

$[Cu_2(tmen)_2(H_2O)_2(\mu\text{-}OH)_2](ClO_4)_2$ (**2**)

The ligand tmen (0.3 mL, 2 mmol) was added to a stirred solution of $Cu(ClO_4)_2{\cdot}6H_2O$ (0.36 g, 1 mmol) in methanol (45 mL). Color of solution turned to dark blue. Solution of H_2tda (0.075 g, 0.5 mmol) with KOH (0.056 g, 1 mmol) in water (4 mL) was added. Little amount of white precipitate was filtered off. After a week violet crystals were collected on a frit funnel, washed with methanol and dried in air. Yield: 220 mg, 70%. Anal. calcd. ($C_{12}H_{38}N_4O_{12}Cl_2Cu_2$): C, 22.9; H, 6.1; N, 8.9 Found: C, 22.8; H, 6.1; N, 8.8%.

2.3. Determination of crystal structure

The dark blue and blue-violet crystals of compounds **1** and **2** (scheme of synthesis and structures of synthesized compounds are shown in Fig. 1A and B) were mounted in turn on a Bruker APEXII automatic diffractometer equipped with charge-coupled device detector, and used for data collection. The compounds were analysed in sealed glass capillaries filled with helium. X-ray intensity data were collected at temperature of 100.0(1) K with microsource (with MonoCap capillary) CuKα (λ = 1.54178 Å) radiation and ω scan mode. The 25 s exposure time was used. The unit cell parameters were determined from 661 and 375 strongest reflections for **1** and **2**, respectively.

Details concerning crystal data and refinement are given in Table 1. An examination of reflections on two reference frames monitored after each 20 frames measured showed no loss of the intensity for both compounds. During the data reduction Lorentz, polarization, and empirical absorption [18] corrections were applied. The structures were solved by partial structure expansion procedure. All the non-hydrogen atoms were refined anisotropically using full-matrix, least-squares technique on F2. All the hydrogen atoms were found from difference Fourier synthesis after four cycles of anisotropic refinement, and refined as "riding" on the adjacent atom with geometric idealization after each cycle of refinement and individual isotropic displacement factors equal 1.2 times the value of equivalent displacement factor of the parent non-methyl carbon or nitrogen atoms and 1.5 times of parent methyl group carbon or oxygen atoms. The methyl groups were allowed to rotate about their local three-fold axis. Some atoms of both compounds show the symptoms of disorder exhibiting in prolating and oblating ellipsoids. The introduction of multipositional disorder models to these atoms, except the one perchlorate anion, does not improve the quality of refinement, thus it can be supposed that this disorder is dynamic in character. The part of one perchlorate anion of compound 2 exhibits the two-domain static disorder (with 6:4 participation of domains) accompanied by further dynamic disorder (the atoms of the both domains still exhibits ellipsoids of revolution). The static disorder is rotational in character, *i.e.* the domains are rotated about local three-fold axis going thought Cl11 and O11 atoms. The SHELXS, SHELXL and SHELXTL [19,20] programs were used for all the calculations. Atomic scattering factors were taken from International Tables for Crystallography.

2.4. Magnetic measurements

Variable – temperature (2 − 300 K) direct current (DC) magnetic susceptibility measurements under applied field of 0.1 ($T < 20$ K) and 1.0 kG ($T \geq 20$ K) and variable – field (0–7 T) magnetization measurements at low temperatures within the range from 2 to 6 K were carried out with Quantum Design SQUID magnetometer. Raw magnetic susceptibility data was corrected for the underlying diamagnetism and the sample holder [7]. Magnetic analyses were carried out by crushing the crystals and restraining the sample in order to prevent any displacement due to its magnetic anisotropy.

2.5. Electron paramagnetic resonance (EPR) spectroscopy

X- (9.5 GHz) and Q-band (35 GHz) EPR measurements were carried out on polycrystalline samples using a Bruker ElexSys E 500 spectrometer and cavities. The measurements were performed in the nitrogen atmosphere at room temperature. The spectrometer was equipped with nuclear magnetic resonance teslameter (ER 036TM) and at X-band frequency counter (E 41 FC). At Q-band as the standard of g-parameter, 1,1-diphenyl-2-picrylhydrazyl was used. Measurements parameters were as follows: microwave power 10 mW, modulation amplitude 8 G, center field 3500 G, range 7000 G for X-band and microwave power 11 mW, modulation amplitude 10 G, center field 11,000 G, range 3990 G for Q-band.

2.6. Fourier-transform infrared spectroscopy (FT-IR)

The middle-infrared (4000–400 cm^{-1}) and far-infrared (600–100 cm^{-1}) spectra were collected on the Fourier-transform, Bruker VERTEX 70V vacuum spectrometer equipped with an air-cooled deuterated triglycine sulfate detector. The copper(II) coordination compounds were placed on the diamond crystal of the attenuated total reflectance accessory. The spectral data were recorded at the resolution of 2 cm^{-1} collection of 128 scans. The spectral data were collected and further elaborated using Bruker OPUS software.

2.7. Theoretical calculations

To perform full geometry optimization, vibrational harmonic frequencies for all molecules were performed by the density functional

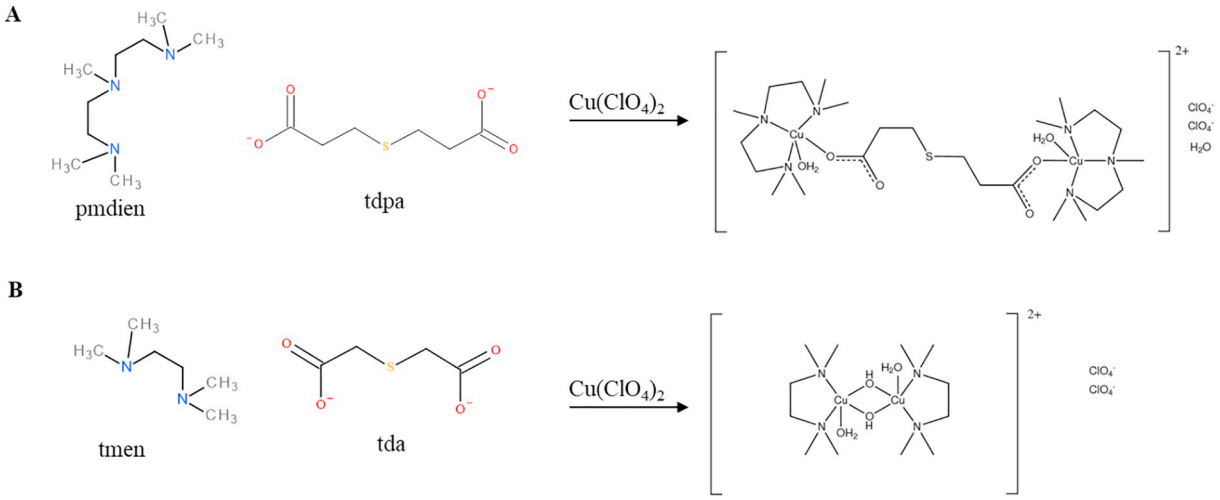

Fig. 1. Syntheses of complexes (A) **1** and (B) **2**.

theory B3LYP-D3 (standard hybrid density functional B3LYP [21,22] method with dispersion correction D3) [23]. This method combined with the basis sets def2-TZVP, for all other atoms, was used to optimize geometry without any symmetry restrictions and wavenumber calculations were carried out to verify whether the optimized molecular structure corresponded to minimum energy. Since the density functional theory (DFT) functional is not able to describe long range London dispersion interactions, we corrected the (semi) local density functional with the original D3 damping function [23]. The DFT calculations of the atomic charges and natural bond orbital (NBO) were performed for the complexes studied [24,25]. The J parameter was calculated at the same level of theory. The calculations were carried out with the Gaussian 09 [26], Orca-ver 4.0 [27] and NBO 6.0 programs [28].

2.8. Cell lines and culture conditions

The human breast cancer cell lines used in this study were: *i*) MDA-MB-231 (ATCC® HTB-26); and *ii*) HBL-100 (ATCC® HTB-124). All cell lines were purchased from Health Protection Agency Culture Collections (Salisbury, UK). Cells were cultured in a RPMI-1640 medium with 10% foetal bovine serum. Media were supplemented with penicillin (100 U/mL) and streptomycin (0.1 mg/mL), and the cells were maintained at 37 °C in a humidified incubator (Eppendorf, Hamburg, Germany) with 5% CO_2. The treatment with copper compounds was initiated after cells reached ~60–80% confluence.

2.9. Testing the effects of *1* and *2* on cellular proliferation

The viability was assayed using MTT (3-(4,5-dimethylthiazol-2-yl)-2,5-diphenyltetrazolium bromide) assay. Briefly, the suspension of 5000 cells in 50 µL medium was added to each well of microtiter plates, followed by incubation for 24 h at 37 °C with 5% CO_2 to ensure cell growth. Treatments with **1** and **2** were carried out for 24 h. Then, 10 µL of MTT [5 mg/mL in phosphate buffered saline (PBS)] was added to the cells and the mixture was incubated for 4 h at 37 °C. After that, MTT-containing medium was replaced by 100 µL of 99.9% dimethyl sulfoxide and, after 5 min incubation, absorbance of the samples was determined at 570 nm using Infinite 200 PRO (Tecan, Maennedorf, Switzerland).

Table 1
Crystal data and structure refinement for **1** and **2**.

Compound	**1**	**2**
Empirical formula	$C_{24}H_{60}Cl_2Cu_2N_6O_{15}S$	$C_{12}H_{38}Cl_2Cu_2N_4O_{12}$
Formula weight	902.82	628.44
Crystal system, space group	Monoclinic, $P2_1/c$ (no. 14)	Monoclinic, $P2_1/c$ (no. 14)
Unit cell dimensions [Å, °]	a = 17.5682(15)	a = 7.6923(5)
	b = 15.5344(10)	b = 14.9129(9)
	c = 14.8028(9)	c = 11.4087(7)
	β = 101.377(2)	β = 108.074(3)
Volume [Å^3]	3960.5(5)	1244.17(14)
Z, Calculated density [mg/m^3]	4, 1.514	2, 1.678
Absorption coefficient [mm^{-1}]	3.655	4.640
F(000)	1896	652
Crystal size [mm]	0.140, 0.120, 0.110	0.093, 0.091, 0.084
θ range for data collection [°]	2.565 to 72.439	5.042 to 72.384
Index ranges	$-21 \le h \le 21$, $-19 \le k \le 18$, $-18 \le l \le 18$	$-9 \le h \le 8$, $-18 \le k \le 18$, $-14 \le l \le 14$
Reflections collected/unique	42,727/7816 [$R_{(int)}$ = 0.0390]	13,244/2457 [$R_{(int)}$ = 0.0318]
Completeness [%] (to θ = 67°)	99.9	99.7
Min. and max. transmission	0.607 and 0.690	0.668 and 0.685
Data/restraints/parameters	7816/0/461	2457/0/176
Goodness-of-fit on F^2	1.099	1.105
Final R indices [$I > 2\sigma(I)$]	$R1$ = 0.0497, $wR2$ = 0.1268	$R1$ = 0.0524, w$R2$ = 0.1392
R indices (all data)	$R1$ = 0.0497, $wR2$ = 0.1268	$R1$ = 0.0526, $wR2$ = 0.1395
Largest diff. peak and hole [e·Å^{-3}]	1.202, −1.248	0.961, −1.004

2.10. Wound-healing assay

For the wound-healing assay, the cells were cultured in 6-well plates until they reached ~80% confluency. Then, a pin was used to scratch and remove cells from a discrete area of the confluent monolayer to form a cell-free zone. After that, cells were re-suspended in a fresh medium enriched with 0.5 mM **1** or **2**, respectively. After 24 h, micrographs of cells were taken and compared with micrographs obtained at 0 h using TScratch software (CSElab, Zurich, Switzerland).

2.11. Fluorescence microscopy of reactive oxygen species (ROS)

Cells were cultivated directly on microscope glass slides (75 × 25 mm, thickness 1 mm, Thermo Fisher Scientific, Waltham, MA, USA) in Petri dishes. After treatment (0.5 mM, 24 h), microscope glass slides with a monolayer of cells were removed from Petri dishes, rinsed with cultivation and directly used for analysis of ROS using CellROX® Green Reagent (Thermo Fisher Scientific) according to manufacturer's instructions. For nuclei counterstaining, Hoechst 33342 was employed. Cells were also visualized under phase contrast (PC). All analyses were carried out using the EVOS FL Auto Cell Imaging System (Thermo Fisher Scientific).

2.12. Single-cell gel electrophoresis (SCGE)

The cells were plated at a density of 10^6 cells/well in six-well dishes and treated with **1** and **2** (0.5 mM) for 24 h. As a control, 150 μM H_2O_2 was employed. After harvesting, app. 15 μL of the cell suspension was mixed with 75 μL of 0.5% low melting point agarose (CLP, San Diego, CA, USA) and layered on one end of a frosted plain glass slide. Then, it was covered with a layer of the low melting agarose (100 μL). After the solidification of the gel, the slides were immersed in a lysing solution (2.5 M NaCl, 100 mM Na_2EDTA, 10 mM Tris, pH 10) containing 1% Triton X-100 and 10% dimethyl sulfoxide), with an overnight incubation at 4 °C. A cold alkaline electrophoresis buffer was poured into the chamber and incubated for 20 min at 4 °C. The electrophoresis was carried at 4 °C, (1.25 V/cm, 300 mA) for 30 min. The slides were neutralized (0.4 M Tris, pH 7.5) and then stained with ethidium bromide (2 μg/mL). The cells were analysed under fluorescence microscope EVOS FL Auto Cell Imaging System (Thermo Fisher Scientific) and classified according to the shape of the fluorescence of the comet tail [0 (*no visible tail*) to 4 (*significant DNA in tail*)].

2.13. Hemocompatibility

Hemocompatibility of **1** and **2** was assayed using human red blood cells (RBCs). Fresh blood sample was withdrawn aseptically by antecubital venipuncture of healthy human donor with signed informed consent. RBCs suspensions were washed with 150 mM NaCl solution three-to-five times. Then, different concentrations of **1** and **2** (0.07–0.5 mM), diluted in PBS were mixed with RBCs and incubated for 1 h at 37 °C. The degree of hemolysis was determined by measuring the absorbance of the supernatant at 540 nm after centrifugation and calculated according to the following equation: $\%hemolysis = [(A_t - A_c) / A_{100\%} - A_c)] \times 100$, where A_t is the absorbance of the supernatant from samples incubated with the 1 and 2; A_c is the absorbance of the supernatant from negative control (PBS, pH 7.4) and; $A_{100\%}$ is the absorbance of the supernatant from positive control (0.1% Triton X-100), which causes complete lysis of RBCs.

2.14. Analysis of an effect of *1* and *2* on protein aggregation

Immediately after blood collection, plasma was isolated from whole blood by centrifugation (3000 × *g*, 5 min). Subsequently, **1** and **2** (0.5 mM in PBS) were incubated in plasma at 1:1 ratio (v/v) in order to mimic the protein concentration *in vivo* (50% plasma in blood). The incubation was done for 35 min at 37 °C under continuous agitation. The protein aggregates were recovered after 10 min centrifugation at 15,000 × *g* and washed three times with cold PBS to remove unbound proteins. Finally, the proteins were eluted by adding sodium dodecyl sulfate (SDS), separated by 12.5% sodium dodecyl sulfate-polyacrylamide gel electrophoresis (SDS-PAGE) and stained by Coomassie brilliant blue. Gels were visualized using Azure c600 (Azure Biosystems, Dublin, CA, USA). Plasma proteins were quantified by densitometric analysis with the AzureSpot software (Azure Biosystems, Dublin, CA, USA).

2.15. Western blotting

Total cellular proteins were extracted upon **1** and **2** treatments (0.5 mM) with radioimmunoprecipitation assay buffer containing protease inhibitor cocktail. After SDS-PAGE, the proteins were electrotransferred onto a polyvinylidene fluoride membrane (Bio-Rad, Hercules, CA, USA) and a non-specific binding was blocked with fresh non-fat milk (1 h at 22 °C). Membranes were incubated with primary mouse anti-MT1/2 (dilution 1:200), mouse anti-MT3 (1:200) mouse anti-p53 (1:250), mouse anti-c-JUN (1:250), mouse anti-Bcl-2 (1:200), mouse anti-MMP-1 (1:200) or mouse anti-GAPDH (1:750), overnight at 4 °C. After washing, the membranes were incubated with rabbit anti-mouse-horseradish peroxidase (HRP) secondary antibodies (Dako, Santa Clara, CA, USA) for 1 h at 20 °C with chemiluminescence detection by Bio-Rad Immun-Star HRP Luminol/Enhancer (Bio-Rad). Membranes were analysed using Azure c600 (Azure Biosystems).

2.16. Determination of antibacterial activities of *1* and *2*

Bacterial cultures [*Staphylococcus aureus* NCTC 8511, *Escherichia coli* NCTC 13216, methicillin-resistant *S. aureus* (MRSA) CCM 7110] were purchased from the Czech Collection of Microorganisms (Brno, Czech Republic). All strains were cultivated in Mueller-Hinton broth (MHB; Oxoid, Hampshire, UK) overnight at 37 °C. The bacterial cultures were diluted with MHB to a concentration ~1 × 10^6 CFU/mL. The bacterial concentrations were normalized by optical density at 600 nm (OD_{600}). The 100 μL of these bacterial suspensions was added into a 96-well microplate and mixed with **1** or **2** in ratio 1:1, with total volume 200 μL. The growth of bacteria suspension with **1** and **2** was monitored by Multiskan EX (Thermo Fisher Scientific). The optical density readouts (OD_{620}) were realized at zero time-point, and then each half-h for 16 h at 37 °C.

Antimicrobial activity was further verified using spread-plate method by inoculating solutions from wells with **1** and **2**. The diluted aliquots were applied onto MHB (Oxoid, Hampshire, UK) plates by spreading a volume of 100 μL and followed by incubation at 37 °C for 24 h.

2.17. Live/dead assay

For live/dead assay the bacterial cultures after the treatment with **1** and **2** were harvested by centrifugation and washed with 0.85% NaCl thrice. Into bacteria solutions fluorescent dyes, SYTO 9 (Thermo Fisher Scientific) and propidium iodide were added and followed by incubation (15 min in dark). Then 5 μL of sample was placed on a glass slide, covered by a glass coverslide and observed with an Olympus IX71 inverted fluorescence microscope (Olympus, Tokyo, Japan).

2.18. Descriptive statistics

For the statistical evaluation of the results, the median was taken as the measurement of the main tendency, while the standard deviation was taken as the dispersion measurement. Differences between groups were analysed using a paired *t*-test. For analyses, Software Statistica 12 (StatSoft, Tulsa, OK, USA) was employed.

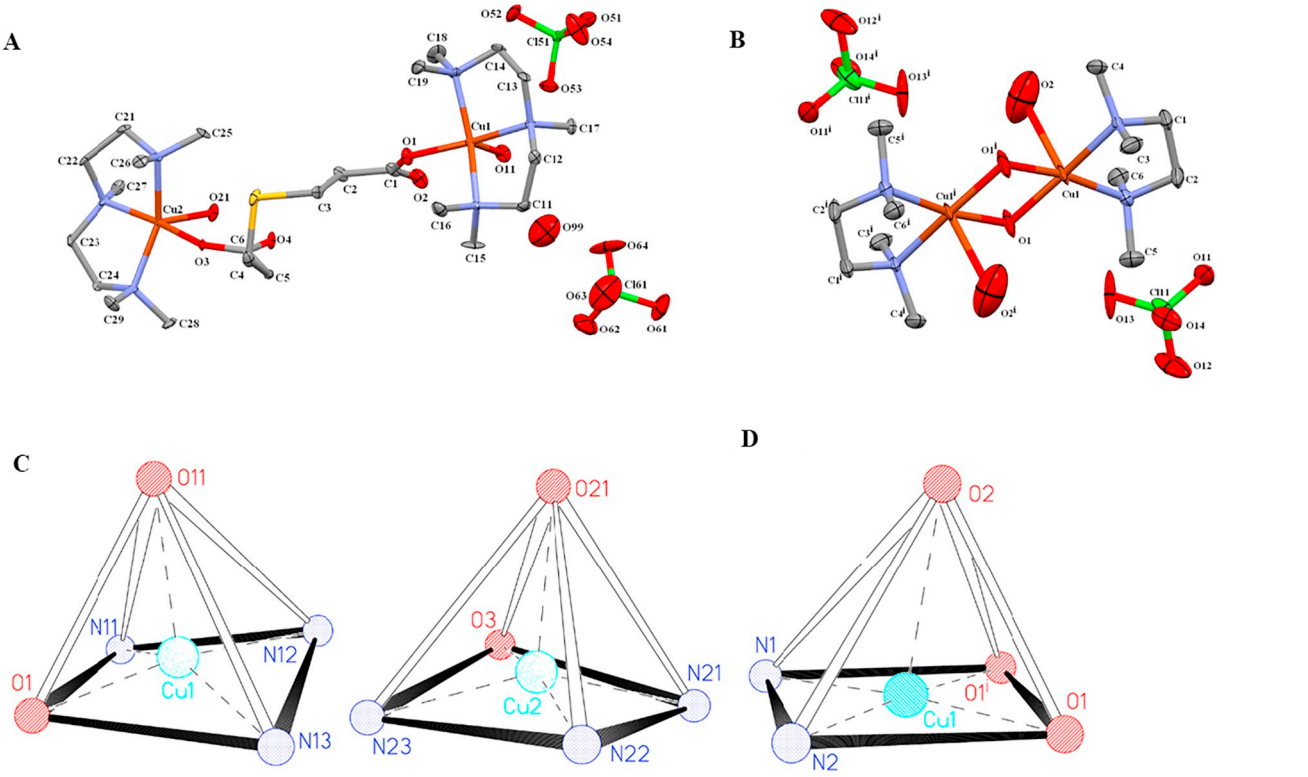

Fig. 2. The molecular structures of (A) **1** and (B) **2** with atom numbering, plotted with 50% probability of displacement ellipsoids. The hydrogen atoms and the disordered domain of **2** are omitted for clarity. The coordination polyhedrons of (C) **1** and (D) **2**.

3. Results and discussion

3.1. Characterization of the structure of 1 and 2

The designed compound **1** with tdpa bridge was successfully synthesized, however similar synthesis in the presence of thiodiacetate anion led to formation of **2** with hydroxo bridges. It can be assumed that potassium salt of the acid and higher amount of tmen form basic conditions, disallowing coordination of tda. Instead of tda bridges, the hydroxo bridges are created in solution. Although central atoms coordination of **2** were already proved [29], the structure was solved at high pressure only and bond lengths are significantly different. Molecular structures of **1** and **2** are shown in Fig. 2A and B. In both compounds, all atoms occupy the general positions. One asymmetric unit of compound **1** contains one dinuclear complex cation, two perchlorate anions and one solvent water molecule. The complex cation of **1** is composed from one bridging difunctional thiodipropionate anion (each carboxylate group acts in monodendate mode), two copper cations, two water molecules and two *N,N,N′,N″,N″*-pentamethyldiethylenetriamine molecules. Each copper ion is five coordinated by one water molecule, three N atoms from pmdien and one O atom of thiodipropionate anion. The existence of the inversion center (special position *a* with multiplicity 2 [30]) at the centroid of the Cu_2O_2 ring core of compound **2** causes that the asymmetric unit contains a half of dinuclear complex cation and one perchlorate anion. The complex cation of **2** consists of two bridging hydroxide anions, two copper cations, two water molecules and two tmen molecules. Each copper ion is five coordinated by one water molecule, one difunctional tmen and hydroxide anions (acting as monodendate ones toward one specific copper cation). The central atom of both compounds exists in the distorted tetragonal pyramid [31] coordination environment (Fig. 2C and D).

The pmdien molecules possess sc^-, ap^+, ap^-, sc^+ conformation, and it agrees with the finding that this conformation is strictly connected with the formation of the tetragonal pyramidal/bipyramidal coordination environment, while sc^-, sc^-, ap^+, sc^- conformation exists for trigonal pyramidal/bipyramidal coordination polyhedra. In addition, the bond valences were computed as $\nu_{ij} = \exp[(R_{ij} - d_{ij}) / b]$ [32,33], where R_{ij} is the bond-valence parameter (in the formal sense R_{ij} can be considered as an parameter equal to the idealized single-bond length between i and j atoms for given b, and theν_{ij} is relative representation of the bond strength [34–36] and b was taken as 0.37 Å [33]. The $R_{Cu\text{-}N}$ and $R_{Cu\text{-}O}$ were taken as 1.735 and 1.654 respectively [37,38]. The computed bond valences (Table S1) show that the weakest is the Cu—OH_2 coordination bond in each inner coordination sphere, and in compound **2** this bond is almost twice weaker than in compound **1**. Oxygen atoms of bridging ligands are bonded to the Cu atoms stronger than the nitrogen atoms of chelating ligands. Total valence of compound **1** Cu atoms is 2.00 v.u. (valence units), and of compound **2** is 2.08 v.u., which proves the correctness of the inner coordination sphere assignment.

The presence of O—H donors in both compounds leads to the formation of classical hydrogen bonds (Table S2). The O—H···O interactions expands the molecules and ions of **1** to the helical chain (Fig. 3) extending along crystallographic [010] plane. The neighboring helixes are interconnected by C—H···O weak hydrogen bonds [39] *via* perchlorate ions to the three-dimensional network. In **2** the O—H···O interactions links the cation and anions and these linkages assemble the ionic species to the three-dimensional supramolecular network. This network is interconnected by multiple C—H···O weak hydrogen bonds (Table S2).

In compound **1** the shortest Cu1···Cu1$^{\#}$ distances in the crystal net are: 8.2973(9), 9.0879(9), 8.8470(6), 8.8470(6), 9.5505(6) and 9.5505(6) Å, respectively. The shortest Cu1···Cu2$^{\#}$ distances in the crystal net are: 8.3198(7), 9.3440(9), 8.4418(9) and 8.1321(7) Å, respectively. In compound **2** Cu1···Cu1$^{\#}$ distances are: 7.6923(5), 7.6923(5), 8.9909(11), 9.1353(11), 2.9829(9), 7.4366(12), 8.1413(6), 8.1413(6), 9.8695(7), 8.0908(8), 8.0908(8) and 9.8695(7), respectively.

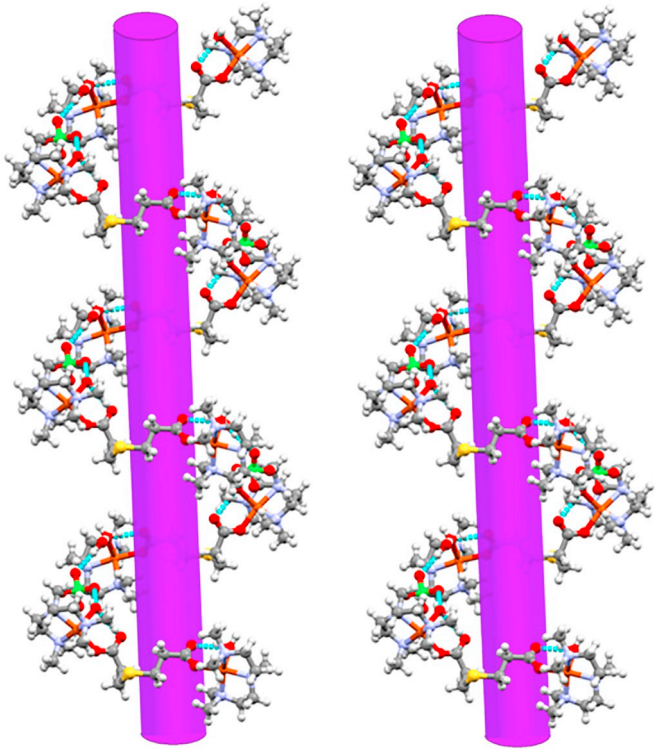

Fig. 3. The part of molecular packing of compound **1**, showing the formation of the supramolecular helical chains.

3.2. Analysis of DC susceptibility

The exchange interaction between two Cu(II) ions ($S_A = S_B = 1/2$) in both compounds was approached to the model of binuclear units realized through thiodipropionate bridge in **1** or bi-hydroxo bridge in **2** together with different additional Cu···Cu contacts transmitted through O—H···O interactions in all compounds. The calculations were based on spin Hamiltonian (Heisenberg-Dirac-Van Vleck) in zero field given in Eq. (1) (SI) describing the isotropic magnetic exchange interaction, antiferromagnetic for $J < 0$ and interaction zJ' between z number of adjacent binuclear units around given binuclear unit in the crystal lattice according to molecular field approximation (MFC) [40]. The experimental magnetic data have been fitted according to Bleaney-Bowers [41] Eq. (2) modified by Eq. (3). shown in Fig. 4.

The temperature independent paramagnetism (TIP) was included also into the fitting procedure. In addition, the presence of different magnetic pathways in the crystal structures of the **1** prompted us to analyze the temperature dependence of the magnetic susceptibility using the alternating Ising chain model, corresponding to the Hamiltonian (Eq. (4)) and the fitting of magnetic data according to Eq. (5) was used (SI).

The magnetic susceptibility data for **1** and **2** were collected over a temperature range of 1.8–300 K under a constant magnetic field of 0.5 T. The temperature dependence of the χ_M, $\chi_M T$ and $1/\chi_M T$ products for **1** and **2** are shown in Fig. 4A and B, respectively. In the case of **1** the χ_M value increases slowly with the decrease of temperature, but at the low–temperature region a rapid increase of molar susceptibility values occurs. The value of $\chi_M T$ at room temperature is 0.82 $cm^3 mol^{-1} K$ (2.56 μ_B), which is slightly higher than expected for spin–only value for two isolated Cu(II) ions (with S = 1/2 and g = 2.00). The $\chi_M T$ value increases systematically with lowering the temperature, reaching 0.88 $cm^3 mol^{-1} K$ (2.65 μ_B) at 5.0 K (Fig. 4A) and then a small decrease up to 0.78 $cm^3 mol^{-1} K$ (μ_{eff} = 2.51 μ_B) is observed at 1.8 K. The compound obeys the Curie – Weiss law in the 5–300 K regions of temperature giving the value of C and Θ constants equal to 0.83 $cm^3 mol^{-1} K$ and 1.92 K, respectively.

Completely different magnetic interaction is observed for **2**. Molar magnetic susceptibility gradually decreases with decreasing temperature to a minimum at 9 K (Fig. 4B). Below this temperature, χ_M increases again due to the presence of paramagnetic impurity, the exact nature of which is unknown. The decrease of magnetic susceptibility is indicative of a strong antiferromagnetic coupling between Cu(II) centers in the Cu_2O_2 moieties. The corresponding plot of $\chi_M T$ value [per two Cu(II) center] *vs.* temperature shows a decrease from 0.403 $cm^3 mol^{-1} K$ (1.80 μ_B) at 300 K (lower than expected for spin–only value for two isolated coper(II) ions with S = 1/2 and g = 2.00) to 0.0075 $cm^3 mol^{-1} K$ (0.24 μ_B) at 1.8 K.

The best agreement with the experimental magnetic data for **1** was obtained with $J = -1 \cdot 10^{-5}\ cm^{-1}$, $zJ' = 0.52\ cm^{-1}$, g = 2.13 and $TIP = 16 \cdot 10^{-6}\ cm^3 mol^{-1}$, $R = \Sigma[(\chi T)exp - (\chi T)calc]2/\Sigma[(\chi T)exp]^2 = 6.81 \cdot 10^{-4}$ (blue lines in Fig. 4A) for **1** and with $J = -186\ cm^{-1}$, $zJ' = -2.01\ cm^{-1}$, g = 2.06, and x = 0.0322 – we add this value according to presence of paramagnetic impurities, $TIP = 116 \cdot 10^{-6}\ cm^3 mol^{-1}$, $R = \Sigma[(\chi T)exp - (\chi T)calc]^2/\Sigma[(\chi T)exp]^2 = 4.81 \cdot 10^{-5}$ (red lines in Fig. 4B) for **2**. The g-values of 2.12 determined by analysis of the magnetic susceptibility data are close to these obtained by simulation of the electron paramagnetic resonance spectra.

The 1-D model used for **1** allows very well fit of the experimental data, slightly better ($R = 6.13 \cdot 10^{-5}$ *vs* $R = 6.81 \cdot 10^{-4}$) than the obtained with Eq. (2), with g = 2.14 and $J_1 = 10^{-5}\ cm^{-1}$, $J_2 = 0.41\ cm^{-1}$, g = 2.13 and $TIP = 18 \cdot 10^{-6}\ cm^3 mol^{-1}$ (red lines in Fig. 4A). The better agreement between the fit and the experimental results seems to give substance to the polymeric vision of the compounds.

Firstly, the value of $|J| \approx 10^{-5}\ cm^{-1}$ for **1** means that the possible exchange path through thiodipropionate bridge is ineffectual due to long Cu···Cu separation of 10.514 Å. Secondly, the value of $zJ' \approx 0.5\ cm^{-1}$ suggested that, the exchange path of ferromagnetic nature, through the hydrogen bonds O—H···O formed between the dimers, which expands the molecules to the helical chain can't be ruled out. The shorter intermolecular Cu···Cu contact are 8.091 and 8.132 Å.

The magnetic behavior of **2** can be explained by the occurrence of magnetic exchange – pathways between Cu(II) pairs. At high temperatures strong antiferromagnetic coupling through oxygen bridges predominates making the $\chi_M T$ values decay, at about 10 K the Cu···Cu pairs almost cancel their spins and plateau is reached. According to literature data (Table S3) concern magnetostructural [42] correlations in dinuclear doubly di-μ-hydroxo-bridged Cu(II) dimers this strong antiferromagnetic interaction present in complex **2** is a result of few structural parameters: the value of Cu—O—Cu angle, φ = 102.48 (3)° (for $\varphi > 97.5°$ the interaction is predicted to be antiferromagnetic, $S = 0$ ground state), Cu—Cu distance of 2.983(1) Å and angular distortions of $LCu(\mu_2\text{-}OH)_2CuL$ which can be expressed by dihedral angle (δ = 177.6°) between the two Cu_2O_2 planes.

However, the quite important intensity of the intermolecular interaction (zJ') in **2** could indicate the presence of a non-negligible second exchange pathway within the material which can be attributed to the presence of O—H···O hydrogen bond in the crystal lattice. Further, the variation of magnetization *versus* magnetic field at 2 K (Fig. 4, right), clearly supports the occurrence of spontaneous magnetic moments in examined complex with Ms. = 1.99 μ_B for **1** and 0.38 μ_B for **2**. In such the cases, the ground state is equal S = 1 and the magnetization should saturate to the value of $M = M_{mol} / (N_A \mu_B) = 2$ at B = 7 T and T = 2.0 K. The obtained value at higher magnetic field for **1** is similar but for **2** drastically smaller and it indicates strong antiferromagnetic interaction between Cu(II) ions.

To rationalize this magnetic behavior, DFT calculations of both complexes have been performed within a broken-symmetry (BS) and high-spin (HS) states [43] framework using the combination of B3LYP and B3LYP-D3 hybrid functionals [see SI] [44–46].

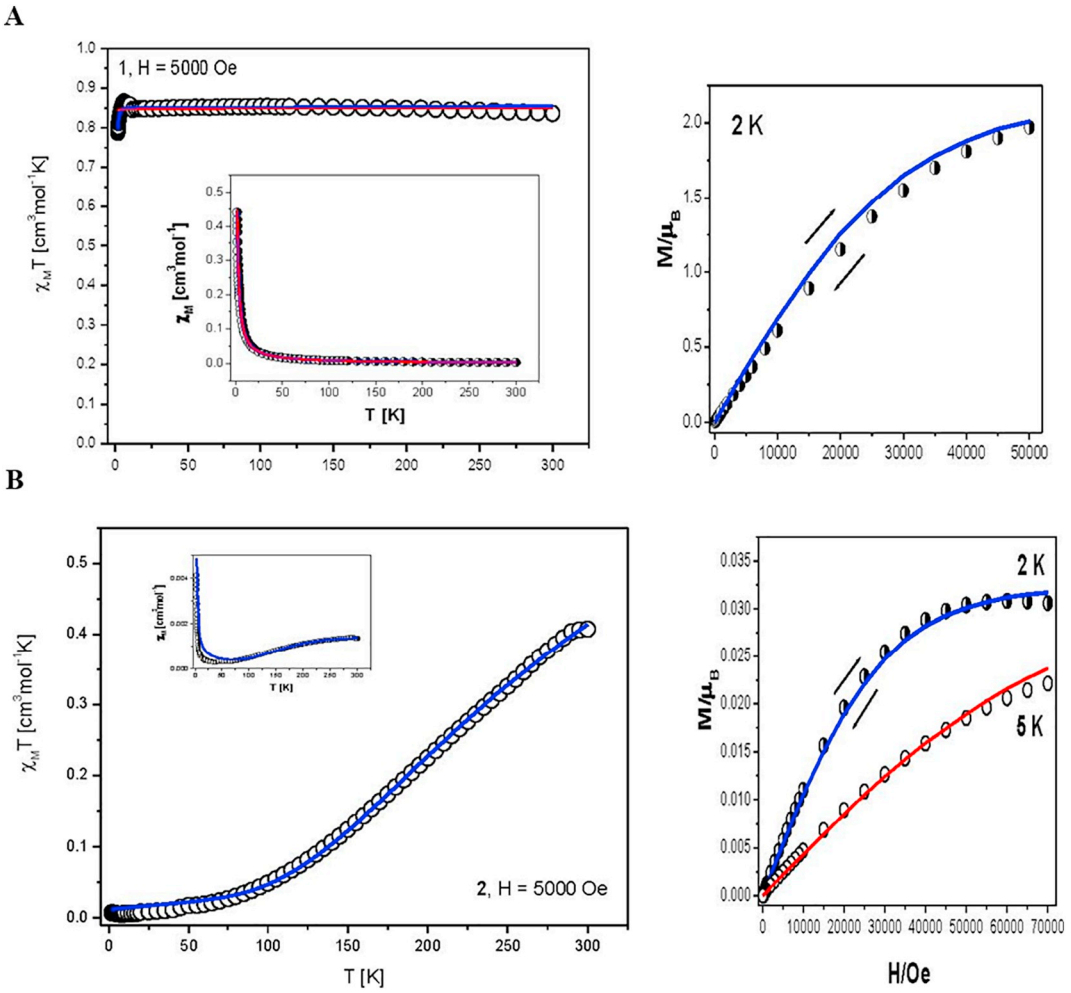

Fig. 4. DC magnetic data for compounds (A) **1** and (B) **2**. Left – temperature dependence of the $\chi_M T$ (inset, molar magnetic susceptibility). The solid blue lines are the curves calculated using Blaeney-Bowers expression. Right – field dependence of the magnetization per formula unit at 2 K (•) and 5 K (o). Lines – fitted.

The obtained results are presented in Table S2. These data clearly show that spin-polarized give the most accurate agreement for examining complexes **1** and **2**. However, due to the strong localization of the wave function at the metal centers, both computational techniques produce results that are in remarkable agreement, both in sign and in the magnitude of the exchange interaction, with the experimental data (Table S2).

In addition to the magnetic coupling constant, it is interesting to pursue natural bond orbital (NBO) analysis applied separately to α and β spin density matrices, as described by Carpenter and Weinhold [47]. These computations were carried out with the Gaussian 09 and NBO 6.0 set of programs. The calculated at the B3LYP-D3/LanL2dz levels of theory the NBO atomic spin densities (Δ) for **1** and **2** in triple state of the $[Cu_2(pmdien)_2(\mu\text{-}tdpa)]_2(H_2O)_2]\cdot(ClO_4)_2$ (**1**), $[Cu_2(tmen)_2(\mu\text{-}OH)_2(H_2O)_2]\cdot(ClO_4)_2$ (**2**) dimer and in doublet state of corresponding monomer, as well as differences between these values, are presented in Table S4 and S5, respectively [see discussion in SI]. The surfaces of the spin density for monomer and dimer discussed are illustrated in Fig. S1.

The values of the energies of the highest occupied molecular orbital (HOMO) and lowest unoccupied molecular orbital (LUMO) orbitals of studied different forms of complexes are collected in the inset of Fig. 5. The DFT energy of HOMO orbital was calculated as −3.820 (for **1**) and −12.688 eV (for **2**). The energy of LUMO orbital of this complex was calculated as −0.909 and −12.444 eV, indicating the energy gap between frontier orbitals of 2.911 and 0.244 eV, respectively. In molecular interaction, the HOMO and LUMO play the key role. HOMO is the orbital, which has ability to donate electrons and its energy corresponds to ionization potential, while LUMO has electrons accepting ability, and its energy corresponds to electron affinity.

B3LYP-D3 calculated interatomic distances, selected bond angles and torsion angles are collected in Table S8 and S9 (numbering compatible with experimental data, see Fig. 2A and B). In the gas phase the crystal packing effects and strong H-bonding interactions are omitted. For the initial geometry in the optimization procedures, the fragment of the crystallographic structure was used. According to the results obtained with respect to the both complexes, the calculated interatomic distances in most cases reflect well the values determined by X-ray. To compare reproducing the experimental interatomic distances and the bond angles for discussed complexes, the corresponding values of the root mean square deviations (RMSD's) were calculated. These values are shown in Table S6 and S7. With regard to these results, there is good compatibility between the results obtained experimentally and those at the DFT level. The value of the RMSD of distances for this complex is 0.148 Å and 0.046 Å, for **1** and **2**, respectively. The analogous situation was noticed for the bond angles. The value of the RMSD is 4.83° and 5.77°, respectively.

3.3. EPR spectra

The polycrystalline EPR spectra of the magnetically concentrated samples were recorded at room temperature and liquid nitrogen temperature Fig. 6. There is no change in the line shape, line width and

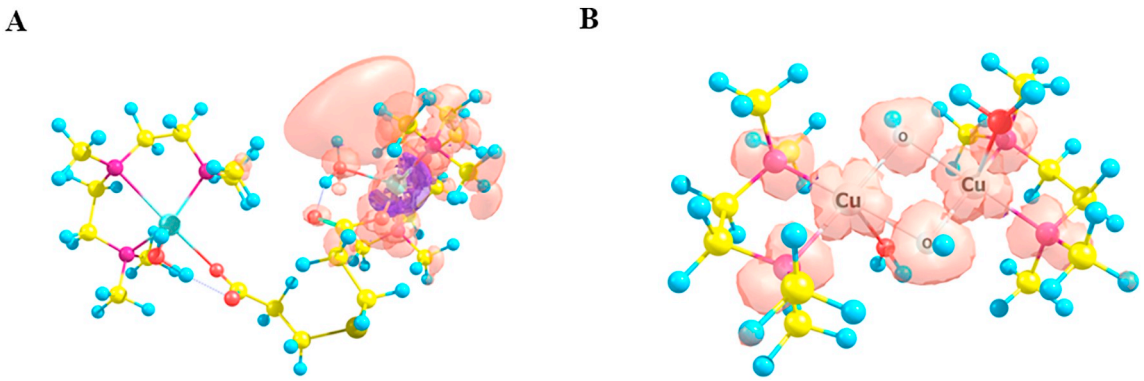

Fig. 5. Spin density surfaces in triple state of: (A) the dimer **1** (see Table S5), (B) the dimer **2** (see Table S6). Orange color corresponds to the positive values of spin density and violet color to the negative values of spin density.

resolution as a function of temperature for **1** (Fig. 6Aa). The anisotropic EPR spectral features can be associated to the axial symmetry having $d_{x^2-y^2}$ ground state, where the geometry can correspond to an elongated octahedral, a square pyramidal or a square planar.

The spectra at Q band present (Fig. 6Ab) signals typical for counter-rotation of neighboring complex molecules around g_z axes [48]. The observed g values $g_1 = 2.165$, $g_2 = 2.129$, $g_3 = 2.057$ (where $g_1 \approx g_z \approx g$ and $(g_2 + g_3)/2 \approx (g_x + g_y)/2 \approx g_\perp$ corresponds to molecular g values) correspond to the orthorhombic symmetry. The individual molecules within the dimer are bridged by thiodipropionic ion, but the dimeric units which can be connected by the axial oxygen atom through hydrogen bond interaction are counted (large torsion angle 116.98°).

The room temperature spectra of **2** at X and Q band show only broad lines typical for axial symmetry ($d_{x^2-y^2}$ ground state). At liquid nitrogen temperature, **2** shows three signals H_1 (3021 mT), H_2 (3200 mT), H_3 (3308 mT) with $g_1 = 2.254$, $g_2 = 2.19$, $g_3 = 2.053$ ($g_{av} = 2.12$) representing a rhombic distortion of the CuO_3N_2 core (Fig. 6Ba). Possible reason for the rhombic-axial discrepancy of the EPR-structural analysis of **2** can be the dynamic Jahn-Teller effect, which causes distortions in the coordination octahedron noticed from non-orthogonal coordination axes and/or different coordinating of oxygen atoms [49].

One question may arise at this juncture regarding the effective species present in solution. In order to correlate the solid and solution structures, we have examined the EPR spectral output of both compounds in frozen solutions (water) and compared to that of the solid samples. The frozen solution EPR spectra of **1** and **2** at 77 K exhibit a well-defined resolution of hyperfine splitting of parallel orientation resulting from the interaction of an unpaired electron with copper nuclei ($I = 3/2$). The spin Hamiltonian parameters are obtained by

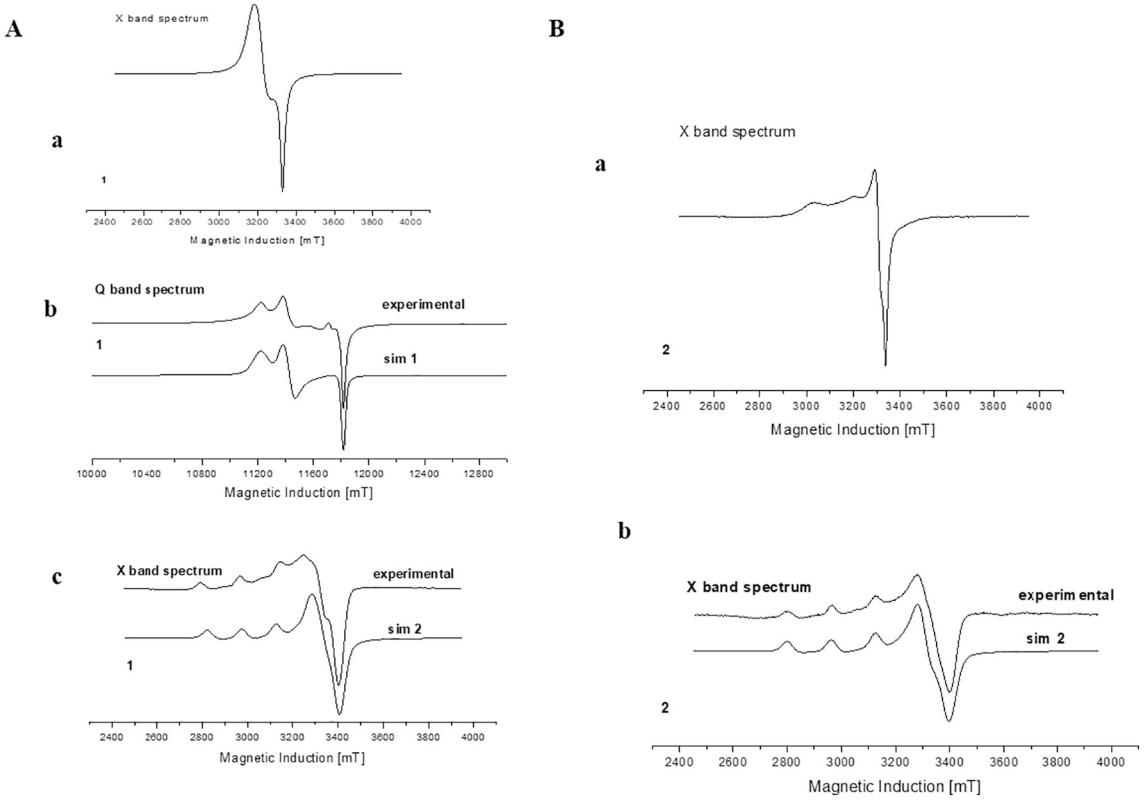

Fig. 6. (A) EPR spectra of: (a) polycrystalline compound at X band **1**; (b) at Q band - experimental and simulated (sim 1), (c) complex **1** frozen solutions in water together with the simulated spectra, sim 2. (B) X band EPR spectra of: (a) polycrystalline compound **2**; experimental and simulated (sim 1) (b) compound **2** frozen solutions in water together with the simulated spectra, sim 2.

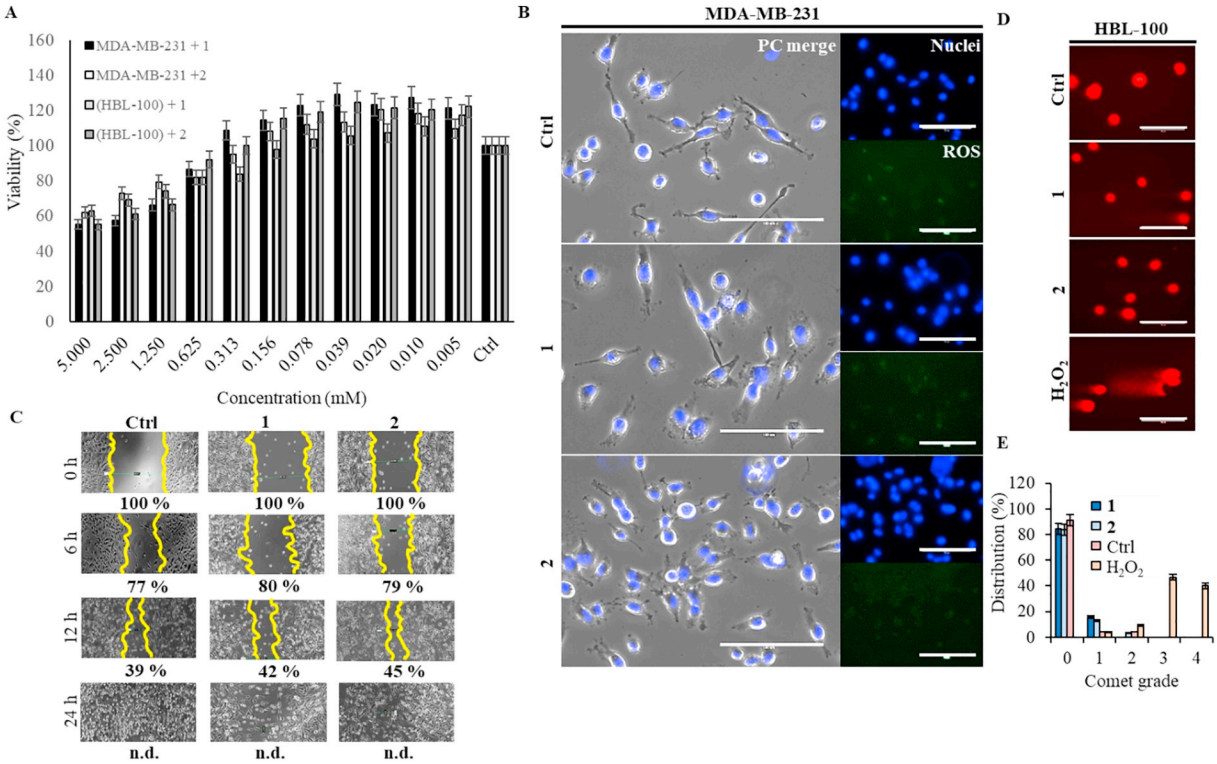

Fig. 7. (A) Cytotoxicity (MTT) screenings showing viability of MDA-MB-231 cell line upon incubation with **1** and **2**. The values are expressed as the mean of six independent replicates (n = 6). Vertical bars indicate standard error. (B) Microscopy analysis showing no deteriorating effects of **1** and **2** on cellular morphology and also no induction of oxidative stress. Scale bar, 100 μm. PC – phase contrast images. (C) Wound-healing assay showing no effect of **1** and **2** on a collective cell migration. The percent indicates the size of a gap related to the control. N.d. – artificial gap not detected. (D) Representative SCGE fluorescence micrographs showing negligible presence of genotoxicity (DNA fragmentation) induced by **1** and **2** in HBL-100 cells. PBS (pH 7.4) and 150 μM H_2O_2 were used as controls. Scale bar, 100 μm. (**E**) Quantitation of index of damage (comet grades). The values are expressed as the mean of three independent replicates (n = 3). Vertical bars indicate standard error.

computer simulation (sim 2 Fig. 6Ac and Fig. 6Bb) of the experimental spectra with $g_x = g_y = g_\perp = 2.041$, $g_z = g_k = 2.24$ and $A_k = 151$ G for **1** and $g_x = g_y = g_\perp = 2.055$, $g_z = g_k = 2.25$ and $A_k = 163$ G for **2**. Hence, the EPR parameters of both complexes in frozen solutions are also consistent with the axial symmetry of the Cu(II) coordination sphere. Furthermore, the change of the parameters upon dissolving **1** and **2** strongly suggests the replacement of the labile oxygen ligands in the binuclear molecule by the solvent molecules in the solutions as was found in many other similar compounds [50,51]. Therefore, if we couple the FT-IR, X-ray and EPR findings, it may be presumed that in **1** and **2**, the dimeric nature exists but with an altered coordination set though the actual composition in solution could not be ascertained.

3.4. FT-IR analysis of *1* and *2*

The FT-IR measurements of **1** and **2** in the middle- and far-IR region are shown in Figs. S1–S4. The calculated vibrational frequencies, as well as the bands observed in the experimental IR spectra along with their assignments, are collected in Table S10 for **1** and in Table S11 for **2**. A detailed vibrational assignment of the experimental spectra has been made on the basis of the potential energy distribution (PED) calculated by the FCART06 program [52] with using B3LYP/def2tzvp level of the theory.

In accordance with the PED, the νO–H(H_2O) band appears as medium peak in spectrum of **1** at 3523 cm^{-1}, but in the experimental FT-IR spectrum of **2** it is not observed (see SI). The aliphatic νC–H stretching vibrations in experimental FT-IR spectrum of **1** are observed as weak bands in the range 3010–2801 cm^{-1} with maximum at 2901 cm^{-1} as well as νC–H in **2**, 2898 cm^{-1}. The characteristic asymmetric stretching vibration corresponding to carboxylate group of thiodipropionate anion (*tdpa*) is observed at 1569 cm^{-1} in the FT-IR spectrum of **1**. Interestingly, the Δ value ($\nu_{as}(COO^-) - \nu_s(COO^-)$) equals to 178 cm^{-1} in **1**, which suggests that the coordination mode of the carboxylate group of *tdpa* is monodentate one [53]. This was confirmed by an X-ray analysis. A similar monodentate type of coordination, was observed for copper(II)-3,3′-thiodipropionate complexes with imidazole, benzimidazole and bipyridine derivatives as well [13–15]. The νC–N, νC–C stretching and δH–N–C bending vibrations of ligand *pmdien* are coupled and they are observed as medium bands in the 1292–919 cm^{-1} range and at 778 cm^{-1} as the sum of the νC–N stretching vibrations. In the IR spectrum of **2** with *tmen* ligand the same type of mode (the νC–N coupled with νC–C) is observed in 1077–936 cm^{-1} range. The next two strong bands and one medium band at 807, 778 and 756 cm^{-1} in the FT-IR spectrum of **2** are the sum of the νC–N stretching vibrations in the two molecules of *tmen* ligand. The band at 808 cm^{-1} in **1** has medium intense absorption and it is due to the δH–O–Cu bending vibrations, the same situation concerns the strong peak at 890 cm^{-1} in FT-IR spectrum of **2**. The strong peak at 622 cm^{-1} in FT-IR spectrum of **1** can be assigned to the vC-C and vC-S stretching vibrations of *tdpa* molecule (calculated 619 cm^{-1}).

The characteristic vibrations of Cu coordination sphere of **1** are formed by the δC1–O1–Cu bending (336 cm^{-1}) and νCu–N (437 cm^{-1}), νCu–O(H_2O) (213 cm^{-1}) stretching vibrations [53]. The νCu–O(tdpa) stretching vibrations are observed at 500 cm^{-1} in FT-IR spectrum of **1**. The interesting breath of Cu_2O_2 ring core in FT-IR spectrum of **2** is observed as medium intense absorption with maxima at 461 cm^{-1} (calculated 460 cm^{-1}). The next medium peak at 449 cm^{-1} in **2** is due to the $\nu Cu1^{i}$-O1 and νCu1-$O1^{i}$ stretching vibrations. The assignment of νCu-N at 242 cm^{-1} is supported by calculations (232 cm^{-1}).

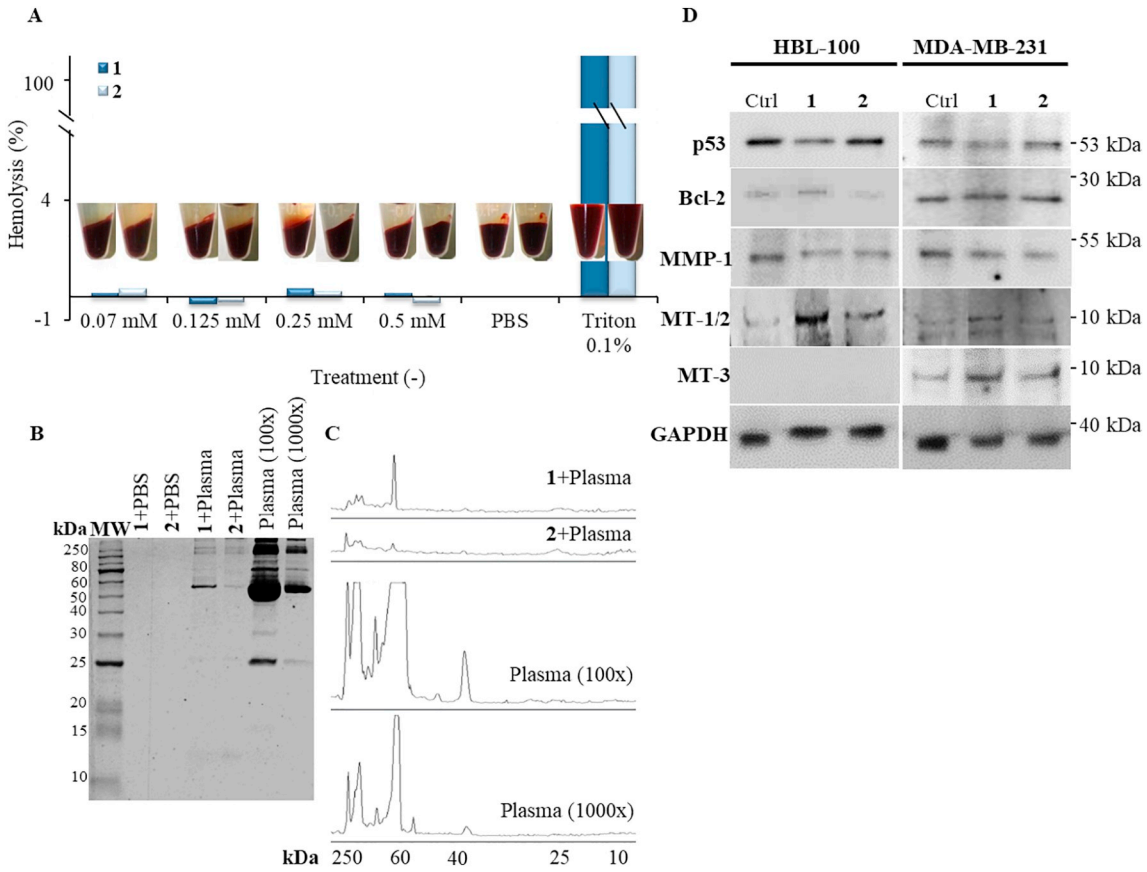

Fig. 8. (A) Hemocompatibility of **1** and **2** assayed on human RBCs. Representative photographs show a clear supernatant above sedimented RBCs in all exposed samples except for positive control (0.1% Triton X-100). (B) Plasma protein aggregation profiles obtained after 1 h incubation of **1** and **2** with human plasma, followed by loading onto 12% SDS-PAGE. MW, Weight marker. (**C**) Resolved protein profiles were analysed using densitometry. (D) Western blots of whole-cell lysates showing effect administration of **1** and **2** on expression of selected proteins. GAPDH - loading control.

3.5. Toxicity studies in mammalian epithelial cells

MDA-MB-231 and HBL-100 cells were cultured in the presence of varying concentrations of **1** and **2** for 24 h. As it can be seen in Fig. 7A, both coordination compounds were cytocompatible, as was also reflected by the fact that under any treatment the 24IC_{50} was not achieved (up to 5 mM concentration). Since copper compounds often induce oxidative stress [54], which can result in DNA mutations and/or DNA damage, we further analysed formation of ROS in tested cells exposed to **1** and **2**. Fig. 7B illustrates that upon 24 h treatment, **1** and **2** did not induce a formation of ROS when compared to non-treated control cells. Moreover, in PC images, it was observed that even upon 24 h exposure, the cellular morphology was not altered and no observable apoptotic morphological features were found. Cytocompatibility of **1** and **2** is also highlighted in Fig. 7C, showing no inhibitory effects on cellular migration. Thus, it can be concluded that in short-term experimental setup the prepared copper compounds do not affect the growth and proliferation of epithelial cell. To confirm exceptional cytocompatibility of **1** and **2**, we further performed SCGE, in which intensity of comet tail relative to the head reflects the number of DNA single- and double-strand breaks in a particular cell. Long comet tails extending toward the anode were observed for cells exposed to positive control only (H_2O_2, Fig. 7D). Using manual scoring (index of damage), 50 randomly selected comets were classified. Fig. 7E illustrates that copper compounds induced a small amount of grade 1 and 2 comets indicating a low amount of DNA damage. Since no ROS induction was found, we anticipate that both copper compounds can bind DNA in small amount (no higher grade comets observed), but without the devastating effects on cellular proliferation.

*3.6. Evaluation of in vitro biocompatibility of **1** and **2** and their effect on expression of selected regulatory proteins*

To characterize the interactions of **1** and **2** with blood environment, we further analysed the copper compounds-induced hemotoxicity and aggregation of plasma proteins. Fig. 8A shows that both compounds are fully hemocompatible without any hemoglobin release. Interestingly, Fig. 8B demonstrates that the incubation of **1** in human plasma resulted in a marked protein aggregation. From densitometry (Fig. 8C), it can be concluded that aggregated proteins are albumins (with approx. 66 kDa) that are the main proteins of blood plasma and commonly bind pharmaceuticals and bioinorganic compounds [55]. Since exposure to metal coordination compounds can alter cellular regulatory mechanisms, we attempted to identify whether **1** and **2** may affect the expression of proteins involved in regulation of cell cycle, apoptosis and response to metals. Noteworthy, Fig. 8D illustrates that we found no **1** or **2**-induced up-regulation of p53 that can be activated by myriad stressors, such as oxidative stress or chemical agents [56]. This fact highlights an exceptional biocompatibility of tested copper compounds. On the other hand, both, **1** and **2** caused subtle down-regulation of MMP-1 that is involved in the breakdown of extracellular matrix in various processes including cancer metastasis [57]. It can be hypothesized that our copper compounds could be useful in combination therapy for metastatic cancers. We are eager to further study this aspect. Moreover, we also identified the stimulatory effects of copper coordination compounds on expression of MT-1/2 and MT-3 that are responsible for metal homeostasis and detoxification [58]. This could be a result of *i*) a direct interaction of **1** and **2** with metal regulatory transcription factor 1 (MTF1) that control expression of MTs and willingly interacts with

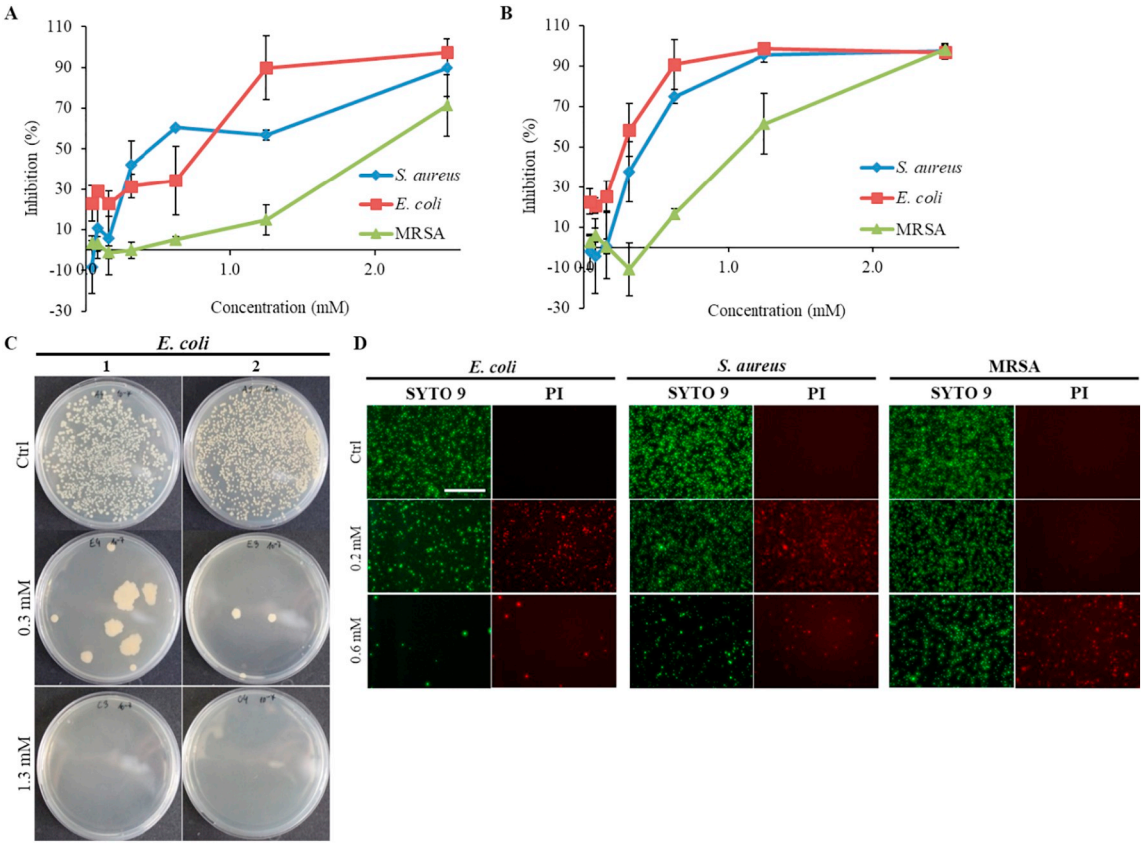

Fig. 9. Growth inhibition of the tested bacterial strains upon incubation with (A) **1** and (B) **2**. The values are expressed as the mean of three independent replicates (n = 3) of growth curve analysis. (C) Representative photographs of *E. coli* plates obtained from spread-plate technique upon incubation with **1** and **2**. (D) Live/dead (SYTO 9/PI) assay showing pronounced antibacterial activity of **2** in all tested bacterial strains. Scale bar, 100 μm.

copper [59], or of *ii*) a competition of **1** and **2** with distinct protein-bound metal ions that are released to cytoplasm and interact with MTF1. Either way, up-regulated MTs presumably help the cells under **1** and **2** exposures to maintain metal homeostasis that leads to a cyto-compatibility of copper compounds. Plausibly, higher concentrations of **1** and **2** would result in a saturation of MTs and in increased cell death. This was evidenced by viability screenings (Fig. 7A).

3.7. Evaluation of the antimicrobial activity of *1* and *2*

Since the synthesized copper compounds exhibited a surprising cytocompatibility in mammalian cells, we further decided to test their toxicity in prokaryotic systems. Some studies show that the Cu(II) compounds exhibit mild antimicrobial activities [2–4]. In line with these results, we found that both, **1** and **2** have similar antimicrobial effects in Gram(+) positive *S. aureus* and Gram(−) negative *E. coli* (Fig. 9A and B, respectively). This fact underpins that an activity of **1** and **2** is not associated with the differences in cell wall structures. Noteworthy, better antimicrobial performance was identified for **2** as also evidenced by spread-plate technique. Representative experiment performed with *E. coli* demonstrated that when exposed to 0.3 mM *E. coli* almost lost its ability to constitute viable colonies (Fig. 9C). This is particularly interesting, since Gram(−) bacteria own mechanisms specialized in the efflux of strange substances out of the cell that inhibiting the action of antimicrobial agents [60]. As **2** showed the best antimicrobial performance, we further validated the obtained results using the Live/dead cell staining (Fig. 9D). The obtained micrographs are in a good agreement with the rest of assays. Importantly, the lowest antimicrobial activity was found for MRSA. MRSA phenotype is mediated by the acquisition of extrachromosomal genetic element SCC*mec* containing the *mecA* gene responsible for resistance to β-lactams [61]. Despite **1** and **2** do not have β-lactam structural feature, it must be noted that different SCC*mec* genotypes confer different resistance characteristics through regulation of distinct resistance and virulence factors present in SCC*mec* cassette [62]. For instance, Cavaco and co-workers identified a putative metal resistance gene in various MRSA isolates of human and animal origin [63]. This finding is not uncommon and a number of studies have described a various metal resistance loci in SCC*mec* [64–66]. A question, which arises, is why the synthesized copper compounds exhibit selective antimicrobial properties. Despite the answer is most likely multifactorial, we anticipate that this phenomenon presumably associates with a bacterial metal homeostasis regulation. In bacteria cytosolic copper levels are typically very low and mostly bound and transported by chaperones that prevent undesired toxicity [67]. As a result of copper over-dosing in bacterial cell, adventitious mismetallation or damage of bacterial chromosomal DNA can occur. However, to prove this hypothesis further studies might follow.

4. Conclusion

The two binuclear Cu(II) coordination compounds containing hydroxy- or thiodipropionate bridge were designed, synthesized and characterized by X-ray crystallography. Moreover, a detailed magnetochemical and EPR study of synthesized compounds was performed. The biological behavior of compounds was studied in a set of experiments comprising either mammalian epithelial cells and distinct bacterial strains. Both compounds were markedly cytocompatible in human epithelial cells. The antimicrobial assays revealed that both compounds exhibit antimicrobial activity regardless the cell wall structure. Despite the mechanism of action of synthesized compounds remains unknown, it most likely associates with metal homeostasis

regulation of prokaryotic cells. Overall, we describe the copper compounds with an interesting selective toxicity and with a promising potential to be further tested in pre-clinical models.

Abbreviations

H_2tda	Thiodiacetic acid
H_2tdpa	Thiodipropionic acid
pmdien	*N,N,N′,N″,N″*-pentamethyldiethylenetriamine
tmen	*N,N,N′,N′*-tetramethylethane-1,2-diamine
MRSA	Methicillin-resistant *Staphylococcus aureus*
DC	Direct current
MFC	Molecular field approximation
TIP	Temperature independent paramagnetism
EPR	Electron paramagnetic resonance
FT-IR	Fourier-transform infrared spectroscopy
DFT	Density functional theory
BS	Broken-symmetry
HS	High-spin
NBO	Natural bond orbital
HOMO	Highest occupied molecular orbital
LUMO	Lowest unoccupied molecular orbital
RMSD	Root mean square deviation
PED	Potential energy distribution
MTT	(3-(4,5-dimethylthiazol-2-yl)-2,5-diphenyltetrazolium bromide
PBS	Phosphate buffered saline
PC	Phase contrast
SCGE	Single-cell gel electrophoresis
RBC	Red blood cell
SDS-PAGE	Sodium dodecyl sulfate-polyacrylamide gel electrophoresis
MT	Metallothioneins
MMP-1	Matrix metalloproteinase 1
GAPDH	Glyceraldehyde 3-phosphate dehydrogenase
HRP	Horseradish peroxidase
MHB	Mueller-Hinton broth
OD	Optical density

Acknowledgements

Financial support from CEITEC 2020 (LQ1601) and ERDF "Multidisciplinary research to increase application potential of nanomaterials in agricultural practice" (No. CZ.02.1.01/0.0/0.0/16_025/0007314) is gratefully acknowledged. The crystallographic part was financed by funds allocated by the Ministry of Science and Higher Education to the Institute of General and Ecological Chemistry, Lodz University of Technology. FT-IR spectroscopy and theoretical calculation was financed by a statutory activity subsidy from the Polish Ministry of Science and Higher Education for the Faculty of Chemistry of Wroclaw University of Science and Technology. We would like to thank Wroclaw Centre of Biotechnology, supporting the EPR and magnetic measurements within the programme of the National Research Centre (KNOW) for years 2014-2018.

Conflict of interest

The authors declare no conflicts of interest.

Appendix A. Supplementary data

Tables of crystal data and structure refinement, anisotropic displacement coefficients, atomic coordinates and equivalent isotropic displacement parameters for non-hydrogen atoms, H-atom coordinates and isotropic displacement parameters, bond lengths and interbond angles have been deposited with the Cambridge Crystallographic Data Centre under No. CCDC1435220 & CCDC1435221 for compounds **1** and **2**, respectively. Supplementary data to this article can be found online at doi: https://doi.org/10.1016/j.jinorgbio.2018.10.011.

References

[1] A.W. Foster, D. Osman, N.J. Robinson, J. Biol. Chem. 289 (2014) 28095–28103.
[2] M.V. Nikolic, M.Z. Mijajlovic, V.V. Jevtic, Z.R. Ratkovic, I.D. Radojevic, L.R. Comic, S.B. Novakovic, G.A. Bogdanovic, S.R. Trifunovic, G.P. Radic, Polyhedron 79 (2014) 80–87.
[3] S. Amer, N. El-Wakiel, H. Ei-Ghamry, J. Mol. Struct. 1049 (2013) 326–335.
[4] A.A.A. Abou-Hussein, W. Linert, Spectrochim. Acta A Mol. Biomol. Spectrosc. 95 (2012) 596–609.
[5] M. Vincent, R.E. Duval, P. Hartemann, M. Engels-Deutsch, J. Appl. Microbiol. 124 (2018) 1032–1046.
[6] W.X. Tian, S. Yu, M. Ibrahim, A.W. Almonaofy, L. He, Q. Hui, Z. Bo, B. Li, G. Xie, J. Microbiol. 50 (2012) 586–593.
[7] A.J. Wilson, V. Geist, International tables for crystallography. Volume C: mathematical, physical and chemical tables, Kluwer Academic Publishers, Dordrecht/Boston/London, 0-792-3-16-38X, 1992 (published for the International Union of Crystallography), 883 Seiten;
Cryst. Res. Technol. 28 (1) (1993) 110.
[8] P. Nagababu, A.K. Barui, B. Thulasiram, C.S. Devi, S. Satyanarayana, C.R. Patra, B. Sreedhar, J. Med. Chem. 58 (2015) 5226–5241.
[9] D. Palanimuthu, S.V. Shinde, K. Somasundaram, A.G. Samuelson, J. Med. Chem. 56 (2013) 722–734.
[10] P. Kopel, Z. Travnicek, J. Marek, M. Korabik, J. Mrozinski, Polyhedron 22 (2003) 411–418.
[11] P. Kopel, Z. Travnicek, J. Marek, J. Mrozinski, Polyhedron 23 (2004) 1573–1578.
[12] A. Bienko, P. Kopel, R. Kizek, R. Kruszynski, D. Bienko, J. Titis, R. Boca, Inorg. Chim. Acta 416 (2014) 147–156.
[13] M. Arici, O.Z. Yesilel, S. Keskin, O. Sahin, O. Buyukgungor, J. Coord. Chem. 66 (2013) 4093–4106.
[14] M. Arici, O.Z. Yesilel, M. Tas, Dalton Trans. 44 (2015) 1627–1635.
[15] M. Arici, O.Z. Yesilel, O. Sahin, M. Tas, Polyhedron 71 (2014) 62–68.
[16] C. Diamante, M.Z. Fiume, W.F. Bergfeld, D.V. Belsito, R.A. Hill, C.D. Klaassen, D.C. Liebler, J.G. Marks, R.C. Shank, T.J. Slaga, P.W. Snyder, F.A. Andersen, Int. J. Toxicol. 29 (2010) 137S–150S.
[17] E. Falletta, C. Della Pina, M. Rossi, Q. He, C.J. Kiely, G.J. Hutchings, Faraday Discuss. 152 (2011) 367–379.
[18] G.M. Sheldrick, *A short history of SHELX*, Acta Crystallogr. Sect. A **64** (2008) 112–122.
[19] G.M. Sheldrick, Acta Crystallogr. 64 (2008) 112–122.
[20] G.M. Sheldrick, Acta Crystallogr. Sect. C-Struct. Chem. 71 (2015) 3–8.
[21] A.D. Becke, J. Chem. Phys. 104 (1996) 1040–1046.
[22] C.T. Lee, W.T. Yang, R.G. Parr, Phys. Rev. B 37 (1988) 785–789.
[23] S. Grimme, J. Antony, S. Ehrlich, H. Krieg, J. Chem. Phys. 132 (2010) 1–7.
[24] D. Avci, Spectrochim. Acta A Mol. Biomol. Spectrosc. 82 (2011) 37–43.
[25] D. Avci, H. Comert, Y. Atalay, J. Mol. Model. 14 (2008) 161–169.
[26] M.J. Frisch, et al., *Gaussian 09, revision A.02*, (2009) Wallingford, CT.
[27] F. Neese, Wiley Interdiscip. Rev.: Comput. Mol. Sci. 2 (2012) 73–78.
[28] E.D. Glendening, J.K. Badenhoop, A.E. Reed, J.E. Carpenter, J.A. Bohmann, C.M. Morales, C.R. Landis, F. Weinhold, Madison, WI, (2013).
[29] A. Prescimone, J. Sanchez-Benitez, K.K. Kamenev, S.A. Moggach, J.E. Warren, A.R. Lennie, M. Murrie, S. Parsons, E.K. Brechin, Dalton Trans. 39 (2010) 113–123.
[30] *International Tables for Crystallography, Volume A: Space Group Symmetry*. 5th Edition ed. 2005, Dordrecht, The Netherlands: Springer.
[31] D.L. Kepert, S.J. Lippard (Ed.), Progress in Inorganic Chemistry, 23 2007, p. 442.
[32] W.H. Zachariasen, J. Less-Common Met. 62 (1978) 1–7.
[33] I.D. Brown, Acta Crystallogr. Sect. B-Struct. Commun. 53 (1997) 381–393.
[34] A. Trzesowska, R. Kruszynski, T.J. Bartczak, Acta Crystallogr. Sect. B: Struct. Sci. 60 (2004) 174–178.
[35] A. Trzesowska, R. Kruszynski, T.J. Bartczak, Acta Crystallogr. Sect. B: Struct. Sci. 61 (2005) 429–434.
[36] A. Trzesowska, R. Kruszynski, T.J. Bartczak, Acta Crystallogr. Sect. B: Struct. Sci. 62 (2006) 745–753.
[37] N.E. Brese, M. Okeeffe, Acta Crystallogr. Sect. B-Struct. Commun. 47 (1991) 192–197.
[38] W.T. Liu, H.H. Thorp, Inorg. Chem. 32 (1993) 4102–4105.
[39] G.R. Desiraju, T. Steiner Journal (1999) Pages.
[40] O. Kahn, *Molecular Magnetism*, VCH, New York, 1993.
[41] B. Bleaney, K.D. Bowers, Proc. R. Soc. Lond. A Math. Phys. Sci. 214 (1952) 451–465.
[42] C.L. Klein, E.D. Stevens, C.J. Oconnor, R.J. Majeste, L.M. Trefonas, Inorg. Chim. Acta 70 (1983) 151–158.
[43] D. Sadhukhan, C. Rizzoli, E. Garribba, C.J. Gomez-Garcia, A. Yahia-Ammar, L.J. Charbonniere, S. Mitra, Dalton Trans. 41 (2012) 11565–11568.
[44] C.F. Macrae, I.J. Bruno, J.A. Chisholm, P.R. Edgington, P. McCabe, E. Pidcock, L. Rodriguez-Monge, R. Taylor, J. van de Streek, P.A. Wood, J. Appl. Crystallogr. 41 (2008) 466–470.
[45] K.B. Yatsimirskii, Pure Appl. Chem. 49 (1977) 115–124.
[46] F.H. Allen, Acta Crystallogr. Sect. B: Struct. Sci. 58 (2002) 380–388.
[47] J.E. Carpenter, F. Weinhold, THEOCHEM J. Mol. Struct. 46 (1988) 41–62.
[48] G. Plesch, C. Friebel, O. Svajlenova, J. Kratsmarsmogrovic, Polyhedron 14 (1995) 1185–1193.

[49] B. Kozlevcar, M.B. Humar, P. Strauch, I. Leban, Z. Naturforsch. B 60 (2005) 1273–1277.
[50] J.C. Jeffery, J.P. Maher, C.A. Otter, P. Thornton, M.D. Ward, J. Chem. Soc. Dalton Trans. 1995 (1995) 819–824.
[51] E. Garribba, G. Micera, D. Sanna, L. Strinna-Erre, Inorg. Chim. Acta 299 (2000) 253–261.
[52] W.B. Collier, I. Magdo, T.D. Klots, J. Chem. Phys. 110 (1999) 5710–5720.
[53] K. Nakamoto, *Infrared and Raman Spectra of Inorganic and Coordination Compounds, Part B*, Wiley & Sons Inc., New York, 2009.
[54] C. Santini, M. Pellei, V. Gandin, M. Porchia, F. Tisato, C. Marzano, Chem. Rev. 114 (2014) 815–862.
[55] N. Singh, D. Pagariya, S. Jain, S. Naik, N. Kishore, J. Biomol. Struct. Dyn. 2017 (2017) 1–14.
[56] H.F. Horn, K.H. Vousden, Oncogene 26 (2007) 1306–1316.
[57] M. Liu, Y. Hu, M.F. Zhang, K.J. Luo, X.Y. Xie, J. Wen, J.H. Fu, H. Yang, Cancer Lett. 377 (2016) 97–104.
[58] L.P. Chen, L. Ma, Q. Bai, X.N. Zhu, J.M. Zhang, Q. Wei, D.C. Li, C. Gao, J. Li, Z.B. Zhang, C.X. Liu, Z.N. He, X.W. Zeng, A.H. Zhang, W.D. Qu, Z.X. Zhuang, W. Chen, Y.M. Xiao, J. Biol. Chem. 289 (2014) 22413–22426.
[59] S.V. Adams, B. Barrick, E.P. Christopher, M.M. Shafer, K.W. Makar, X.L. Song, J.W. Lampe, H. Vilchis, A. Ulery, P.A. Newcomb, Toxicol. Appl. Pharmacol. 289 (2015) 381–388.
[60] D.G. Brown, T.L. May-Dracka, M.M. Gagnon, R. Tommasi, J. Med. Chem. 57 (2014) 10144–10161.
[61] F.D. Lowy, J. Clin. Invest. 111 (2003) 1265–1273.
[62] C. Kaito, Y. Saito, G. Nagano, M. Ikuo, Y. Omae, Y. Hanada, X.A. Han, K. Kuwahara-Arai, T. Hishinuma, T. Baba, T. Ito, K. Hiramatsu, K. Sekimizu, PLoS Pathog. 7 (2011) 1–18.
[63] L.M. Cavaco, H. Hasman, M. Stegger, P.S. Andersen, R. Skov, A.C. Fluit, T. Ito, F.M. Aarestrup, Antimicrob. Agents Chemother. 54 (2010) 3605–3608.
[64] S. Monecke, L. Jatzwauk, E. Muller, H. Nitschke, K. Pfohl, P. Slickers, A. Reissig, A. Ruppelt-Lorz, R. Ehricht, PLoS One 11 (2016) 1–24.
[65] M.A. Argudin, B. Lauzat, B. Kraushaar, P. Alba, Y. Agerso, L. Cavaco, P. Butaye, M.C. Porrero, A. Battisti, B.A. Tenhagen, A. Fetsch, B. Guerra, Vet. Microbiol. 191 (2016) 88–95.
[66] S. Baig, T.B. Johannesen, S. Overballe-Petersen, J. Larsen, A.R. Larsen, M. Stegger, Infect. Genet. Evol. 61 (2018) 74–76.
[67] P. Chandrangsu, C. Rensing, J.D. Helmann, Nat. Rev. Microbiol. 15 (2017) 338–350.